Automatic Off-Resonance Correction in Spiral Imaging With Piecewise Linear Autofocus

Travis B. Smith,* and Krishna S. Nayak

Off-resonance generates blurring artifacts in spiral images. Applications that often utilize spiral trajectories, such as fine-resolution imaging and rapid scanning, typically preclude the measurement of accurate field maps needed for effective off-resonance correction. Automatic deblurring, or autofocus, algorithms have been developed to estimate the field map directly from the corrupted data prior to off-resonance correction, eliminating the need for field map measurements. These algorithms rely in whole or in part on optimizing an objective function, and suffer from problems related to the accurate minimization and utility of the function. Here, a new method is presented to correct off-resonance blurring automatically without an objective function using a piecewise linear framework. Local linear field maps are estimated with a combination of *k*-space spectral analysis and mapdrift, an image feature-based correlation technique, for subsequent piecewise linear deblurring. This approach enables field map estimation without optimization, provides accurate off-resonance correction, is suitable for low signal-to-noise ratio and fine-resolution applications, and does not require access to the raw data. Deblurred images from fine-resolution spiral scans of a phantom and healthy volunteers at 3T show that the proposed method can be superior to conventional autofocus and comparable to field map-based correction. **Magn Reson Med 69:82–90, 2013. © 2012 Wiley Periodicals, Inc.**

Key words: spiral; automatic deblurring; off-resonance correction; autofocus

With spiral imaging, a significant advantage and a critical weakness share the same underlying cause. The two-dimensional variation along each spiral readout enables full utilization of the gradient hardware and provides time-efficient *k*-space coverage. However, it also generates radially increasing *k*-space phase errors in the presence of off-resonance, causing blurring and distortion of the reconstruction kernel. Shorter readout times reduce these errors but necessitate additional spiral arms and longer scan times, negating the time-efficiency benefit.

Several methods have been developed to correct off-resonance blurring using a measured field map of the spatial distribution of off-resonance frequencies (1–5). As these strategies typically apply locally zeroth-order correction via pixel-by-pixel center frequency adjustments, they require the field map to be nearly constant across the width of the point spread function. Consequently, they can correct spatially smooth phase errors, which often occur with B_0 field inhomogeneity but may not accurately model susceptibility and chemical changes around tissue interfaces. More importantly, the deblurring effectiveness is limited by the fidelity of the measured field map, which may be inaccurate due to signal loss, subject motion, phase wraps, or poor resolution including intrinsic blurring artifacts. Measuring an accurate field map requires additional scan time and is often infeasible in fine-resolution and time-sensitive imaging experiments.

Automatic deblurring (autofocus) methods estimate the field map directly from the acquired data before compensating the phase errors. Current techniques (6–9) rely in varying degrees on optimizing a focus metric. The optimization has usually been some variant of minimizing the imaginary image, first proposed by Noll et al. (6), which can be inaccurate because of false minima. Improvements to the focus metric (10) and augmentation with low-resolution field map information (11) have been suggested, but the metrics still require the prescient removal of all image phase unrelated to the off-resonance and generally lack robustness. The KESA approach by Truong et al. (9) is notable for its incorporation of a signal physics model to supplant, at least partially, the reliance on a focus metric. In essence, these optimization-based autofocus methods have replaced the limitations stemming from field map inaccuracy with limitations of the focusing metric. Autofocus techniques have been mostly restricted to low-resolution or low field strength applications.

In this study, we present an automatic off-resonance correction algorithm, called piecewise linear autofocus, that does not use focus metrics. As with (4), it performs block-based processing of the blurry image, but instead estimates a piecewise linear field map using signal physics and then performs locally first-order correction. Compared to other autofocus algorithms, the piecewise linear framework in the proposed method enables field map estimation without a focus metric, more accurately corrects rapidly varying off-resonance, and provides noise robustness—which is important for fast and fine-resolution scans with low signal-to-noise ratio (SNR). Spiral imaging experiments with phantom and volunteer data at 3T indicate that the proposed autofocus technique can be superior to conventional autofocus and comparable to conventional field map-based deblurring.

THEORY

The primary stages of the piecewise linear autofocus algorithm are field map estimation, field map smoothing, and off-resonance correction (Fig. 1). The algorithm, which requires as inputs only the blurry complex image and the trajectory time map, divides the image into blocks

Ming Hsieh Department of Electrical Engineering, University of Southern California, Los Angeles, California, USA.

Grant sponsor: The American Heart Association.

*Correspondence to: Travis B. Smith, M.S.E., Ming Hsieh Department of Electrical Engineering, University of Southern California, 3740 McClintock Avenue, EEB 412, Los Angeles, CA 90089-2564. E-mail: traviss@usc.edu

Received 2 December 2011; revised 20 January 2012; accepted 5 February 2012.

DOI 10.1002/mrm.24230

Published online 27 March 2012 in Wiley Online Library (wileyonlinelibrary.com).

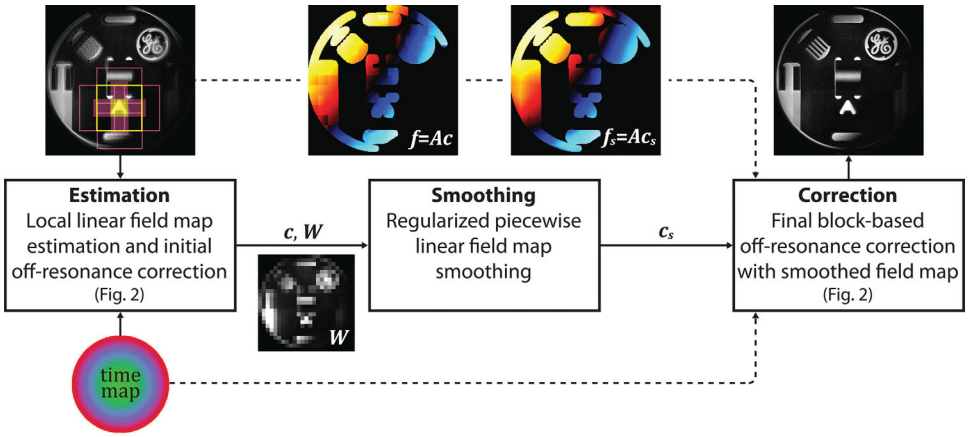

FIG. 1. Overview of the proposed algorithm. After each block undergoes estimation, the local coefficients (***c***) and weights (***W***) are used to smooth the discontinuous piecewise linear map (***f***). Linear off-resonance correction is then applied to the blocks with the coefficients ($\boldsymbol{c}_s$) from the smoothed field map ($\boldsymbol{f}_s$). [Color figure can be viewed in the online issue, which is available at wileyonlinelibrary.com.]

and performs automatic linear field map estimation and correction on each block before recombining them into the final image. Prior to correction, the individual linear field maps from each block are joined into a piecewise linear field map, which undergoes regularized smoothing to minimize artifacts from discontinuities along the block boundaries. The next sections describe the linear off-resonance model, estimation strategy, and details of the piecewise linear processing framework.

Linear Off-Resonance

Neglecting relaxation, off-resonance, coil sensitivity and noise, the signal equation for an MR scan of an object with spin density $m(x,y)$ is

$$s(t) = \int\int m(x,y)e^{-j2\pi(k_x(t)x+k_y(t)y)}\mathrm{d}x\mathrm{d}y, \qquad [1]$$

where $k_x(t)$ and $k_y(t)$ are the x and y and components of the k-space trajectory at time t. The time map for a nonoverlapping k-space trajectory is denoted by $t(k_x,k_y)$ and can be useful in rewriting the signal in terms of frequency coordinates, $s(t) = s(t(k_x,k_y)) = s(k_x(t),k_y(t)) = s(k_x,k_y)$.

Off-resonance adds a space- and time-varying phase term to the signal equation. Letting $f_o(x,y)$ be the spatial distribution of off-resonance in Hz, the corrupted signal s_o is

$$s_o(k_x,k_y) = \int\int m(x,y)e^{-j2\pi(k_xx+k_yy)}e^{-j2\pi f_o(x,y)t(k_x,k_y)}\mathrm{d}x\mathrm{d}y. \qquad [2]$$

If the off-resonance is modeled with an affine field then $f_o(x,y) = f_c + f_xx + f_yy$, where f_c, f_x, and f_y represent the constant and linear field coefficients. With this model, the signal equation becomes

$$s_o(k_x,k_y) = e^{-j2\pi f_ct}\int\int m(x,y)e^{-j2\pi[(k_x+f_xt)x+(k_y+f_yt)y)]}\mathrm{d}x\mathrm{d}y \qquad [3]$$

in which the k-space dependence of the time map has been hidden to improve clarity. The corrupted signal s_o can be expressed in terms of the ideal signal s by combining Eqs. 1 and 3.

$$s_o(k_x,k_y) = e^{-j2\pi f_ct}s(k_x+f_xt,k_y+f_yt). \qquad [4]$$

Equation 4 reveals the effects of the off-resonance components. The linear coefficients cause a time-varying shift of the k-space trajectory that will manifest as image distortion and warping. The constant component produces a k-space phase modulation. For spiral trajectories, the time map is approximately quadratic with k-space radius, and this modulation becomes a quadratic phase error that broadens (blurs) the point spread function.

Automatic Linear Off-Resonance Estimation

We assume a piecewise affine model for the field map and estimate the local constant and linear coefficients in each block of image pixels. Figure 2 shows a diagram of the estimation steps for a block. Blocks are specified by their field of view $\mathrm{FOV_b}$ and are arranged in tight adjacency. Blocks are padded with neighboring pixels to size $\mathrm{FOV_p}$ to improve estimation accuracy and mitigate blocking artifacts in the image. The padded regions are discarded when processed blocks are recombined. In the estimation stage, padded blocks are premultiplied with a Gaussian window to emphasize the signal from the inner region and reduce contamination from neighboring blocks. The k-space data for each block are accessed through the 2D fast Fourier transform at Cartesian frequency locations (k'_x,k'_y). The trajectory time map, which preserves the temporal characteristics of the spiral trajectory, is linearly interpolated from $t(k_x,k_y)$ to $t(k'_x,k'_y)$ prior to processing.

We first estimate the local linear field map coefficients for the block. Denoting the k-space data for a particular block as $s_o(k'_x,k'_y)$, Eq. 4 can be rewritten as

$$s(k'_x,k'_y) = e^{+j2\pi f_ct}s_o(k'_x-f_xt,k'_y-f_yt). \qquad [5]$$

At the echo time t = TE, the gradient-induced phase shifts across the object become zero and a gradient echo causes a signal peak. From Eq. 5, the magnitude spectrum at the echo time becomes

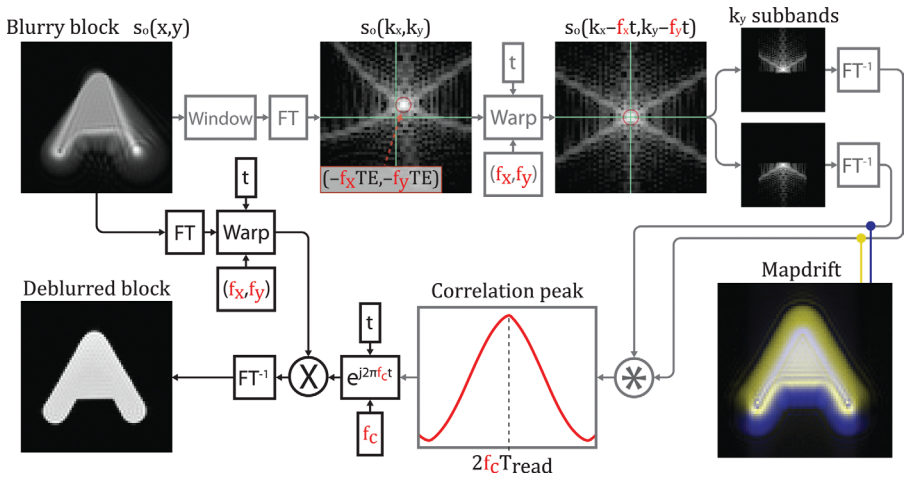

FIG. 2. Flow chart of the linear field map estimation (gray) and correction (black) performed on each block. The local linear coefficients (f_x,f_y) are estimated from the spectral peak location, and the constant coefficient (f_c) is estimated with the mapdrift technique. Mapdrift processing is performed along both the *x* and *y* directions, but only the latter is shown. Reconstructed sub-band images (yellow and blue) are superimposed to demonstrate the differential translation detected by mapdrift. The smoothed coefficients are used for the final correction. [Color figure can be viewed in the online issue, which is available at wileyonlinelibrary.com.]

$$|s(0,0)| = |s_o(-f_x\mathrm{TE}, -f_y\mathrm{TE})|, \quad [6]$$

which isolates the linear coefficients and relates them to the location of the signal peak. If the peak of the acquired signal s_o occurs at *k*-space location $(\upsilon'_x, \upsilon'_y)$, then the linear field map coefficients can be estimated with

$$f_x = -\upsilon'_x/\mathrm{TE} \text{ and } f_y = -\upsilon'_y/\mathrm{TE}. \quad [7]$$

We measure the peak location after Fourier transforming the block with zero-padding, which sinc-interpolates the *k*-space data to increase the localization precision. Estimating the linear coefficients from the spectral peak is related to susceptibility gradient mapping (12) and the KESA method for spiral image deblurring (9). With KESA, large energy changes are detected at each image pixel in response to varying the frequency support of a partial Fourier reconstruction. In comparison, our block-based approach has improved robustness because it uses more samples—all pixels in the block—to form each estimate and operates in the frequency domain where the spectral peak is directly observable.

Before estimating the constant coefficient, the trajectory shift is corrected to properly align the *k*-space data with the time map. The *k*-space data for the block are resampled from Cartesian grid locations (k'_x, k'_y) to shifted locations $(k'_x - f_x t, k'_y - f_y t)$. We perform this operation by regridding the block's *k*-space data with uniform density compensation. Note that there is no advantage to estimating the constant coefficient before the linear coefficients because the former involves only the frequency-domain phase and does not influence the location of the peak magnitude.

After the trajectory shift has been corrected, the constant coefficient is estimated with the mapdrift technique (13), which measures super-linear phase errors by examining the drift between images reconstructed from two separate sub-bands. As the f_c-induced phase error is approximately quadratic along a spoke in *k*-space (Fig. 3a), each half of the spoke, or sub-band, has a strong but opposite linear phase modulation that causes an equal but opposite translation in the image domain (Fig. 3b). Measuring this differential translation, or drift, by correlating the sub-band images produces an estimate of the quadratic phase error amplitude. To adapt the mapdrift technique to spiral MRI data, we form sub-bands from *k*-space strips of width *B* (Fig. 3c). We measure the drift twice—along *x* and *y*—with low-resolution sub-band images and average the results. For example, to measure the drift in the *y*-direction, we first extract the strip defined by $|k'_x| \le B/2$ from $s_o(k'_x - f_x t, k'_y - f_y t)$ and then form two sub-bands defined by $k'_y \ge -\kappa$ and $k'_y \le \kappa$ (corresponding, respectively, to the blue and yellow outlined regions in Fig. 3d). Each sub-band image is reconstructed by inverse Fourier transformation before undergoing cross-correlation to measure the drift. The f_c coefficient is estimated from the lag corresponding to the correlation peak, which in the absence of errors will be $2f_c T_{\mathrm{read}}$, where T_{read} is the spiral readout duration.

Sub-band images are reconstructed with the FFT which, although computationally efficient, has basis vectors that do not follow the circular symmetry of the phase error. During inverse Fourier transformation, projections along the Cartesian axes result in phase averaging, reduction of the aggregate phase error amplitude, and a diminished linear phase differential between the sub-bands. The drift will be attenuated by a factor of α, with $0 < \alpha \le 1$, that depends on the sub-band size and distribution of *k*-space energy, and causes f_c underestimation.

The sub-band size is chosen to balance this attenuation with the effectiveness of the correlation. Attenuation is minimized with the smallest possible sub-bands, defined by $B = 1/\mathrm{FOV_p}$ (narrow) and $\kappa = 0$ (nonoverlapping), so that α is near unity. Increasing the width *B* yields finer sub-band image resolution and reveals more features to correlate, but increases the phase averaging during projection and reduces α (Fig. 3e). Increasing the overlap κ leverages the natural apodization of the

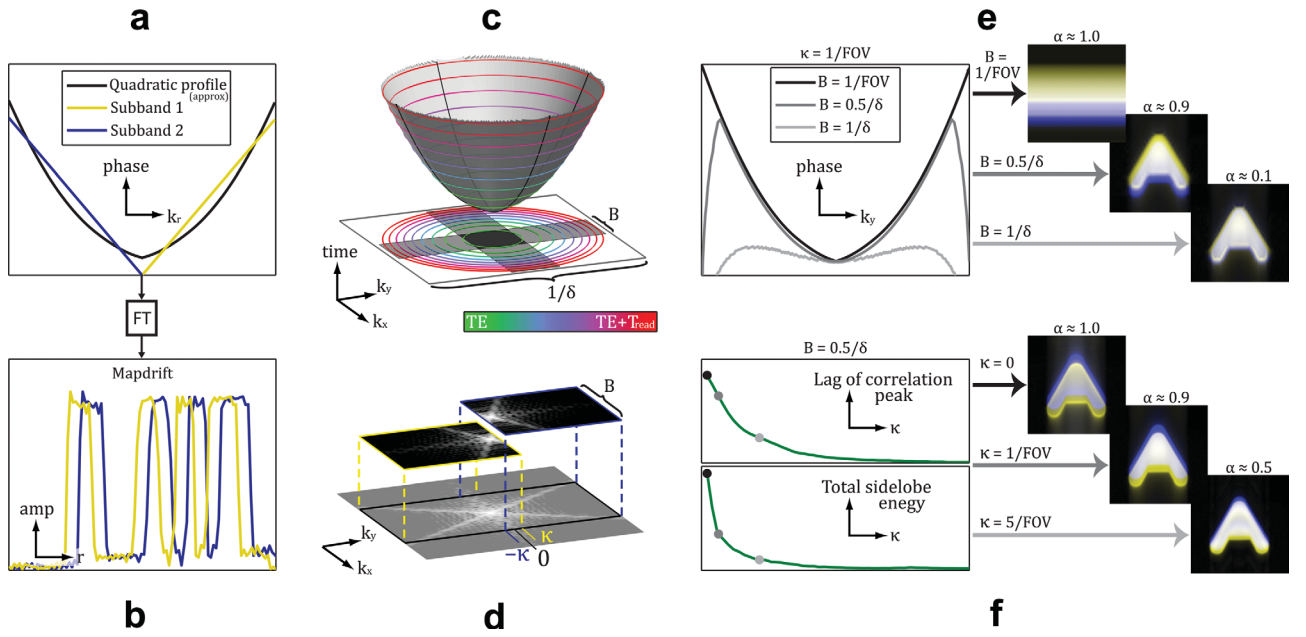

FIG. 3. The mapdrift technique estimates super-linear phase errors. **a**: Dividing the spectrum into two sub-bands creates strong but opposite linear phase components (yellow and blue) from the approximately quadratic phase error (black). **b**: Reconstructing the sub-bands produces a differential translation that is proportional to the phase error and measured with correlation. **c**: In spiral imaging, off-resonance will generate a quadratic phase error and point spread function blurring because the trajectory time map is approximately quadratic with *k*-space radius. To measure the phase error, we perform mapdrift processing using two strips of *k*-space data of width *B* ($0 < B = 1/\delta$ with δ = image resolution). **d**: Each strip is divided into two sub-bands that are overlapped by κ before being reconstructed into images and correlated. **e**: The effect of *B* on mapdrift accuracy. Smaller *B* reduces sub-band image resolution but better preserves the quadratic phase profile across the strip. **f**: The effect of κ on mapdrift accuracy. Larger κ reduces energy from interfering sidelobes, but also reduces the differential translation and shifts the peak correlation lag toward zero.

k-space data to mitigate interference from sidelobes during correlation, but reduces the phase difference between the sub-bands (Fig. 3f). We experimented with various sub-band sizes to balance these diametric behaviors and achieved good results with $B = 0.5/\delta$, where δ is the image resolution, and $\kappa = 1/\mathrm{FOV_p}$, meaning one overlapping frequency in addition to DC.

Individual calibrations could be performed for each block to measure α and correct the underestimation. To reduce computational overhead, we instead estimate f_c iteratively. Starting with an initial estimate of zero, we compensate the f_c-induced error in the block with a conjugate phase multiplication by $\exp(j2\pi f_c t)$ and then perform mapdrift to update the estimate, repeating these steps until convergence. Depending on the anatomical features and residual off-resonance in the block, the estimate may oscillate between frequencies; in this situation, we assign the average frequency to the estimate. We are currently investigating the suitability of polar Fourier transforms as an alternative for more efficient mapdrift estimation.

After mapdrift processing, the trajectory-adjusted and phase-compensated *k*-space data for the block are reconstructed with inverse Fourier transformation to produce an initially corrected image block.

Field Map Smoothing

As the blocks are processed independently, combining them after initial correction could produce image artifacts similar to those observed in other block-based approaches (4). The combined piecewise linear field map could also have discontinuities along the block boundaries. To minimize these discontinuities and the associated image artifacts, we smooth the combined field map while maintaining its piecewise linearity and then perform the final off-resonance correction with the smoothed map.

The combined field map is smoothed within a piecewise linear subspace by penalizing the discontinuities along the (unpadded) block boundaries. The original field map estimate $\boldsymbol{f}$ is factored into a piecewise linear basis $\boldsymbol{A}$ and coefficient vector $\boldsymbol{c}$ so that $\boldsymbol{f} = \boldsymbol{A}\boldsymbol{c}$. For an $N \times N$ image that has been divided into a total of M blocks, $\boldsymbol{f}$ is $N \times N$, $\boldsymbol{A}$ is $N^2 \times 3M$, and $\boldsymbol{c}$ is $3M \times 1$. We perform the smoothing by solving the following Tikhonov regularization problem (14)

$$\min_{\boldsymbol{c_s}} ||\boldsymbol{f_s} - \boldsymbol{f}||^2_{2,\mathbf{w}} + \lambda\left(||\boldsymbol{D_x}\boldsymbol{f_s}||^2_2 + ||\boldsymbol{D_y}\boldsymbol{f_s}||^2_2\right) \quad [8]$$

for the smoothed coefficients $\boldsymbol{c_s}$, where $\boldsymbol{f_s} = \boldsymbol{A}\boldsymbol{c_s}$ is the smoothed field map. The first term in Eq. 8 is a weighted penalty for the smoothing error. The diagonal weighting matrix $\boldsymbol{W}$ is formed from the initially corrected blocks and contains the average image intensity for the block to which each pixel belongs (Fig. 1). The second term penalizes discontinuities along the block boundaries using second-order difference operators $\boldsymbol{D_x}$ and $\boldsymbol{D_y}$.

Equation 8 is convex and has the analytical solution $\boldsymbol{c_s} = (\boldsymbol{A}^{\mathrm{T}}\boldsymbol{W}\boldsymbol{A} + \lambda\boldsymbol{D})^{-1}\boldsymbol{f}$, found by gradient minimization (14). This yields the following expression for the smoothed field map

$$\boldsymbol{f_s} = \boldsymbol{A}(\boldsymbol{A}^{\mathrm{T}}\boldsymbol{W}\boldsymbol{A} + \lambda\boldsymbol{D})^{-1}\boldsymbol{f}. \quad [9]$$

Here, $\boldsymbol{D} = \boldsymbol{A}^{\mathrm{T}}(\boldsymbol{D}_{\boldsymbol{x}}^{\mathrm{T}}\boldsymbol{D}_{\boldsymbol{x}} + \boldsymbol{D}_{\boldsymbol{y}}^{\mathrm{T}}\boldsymbol{D}_{\boldsymbol{y}})\boldsymbol{A}$ and $\boldsymbol{A}^{\mathrm{T}}\boldsymbol{W}\boldsymbol{A} + \lambda\boldsymbol{D} \succ \boldsymbol{0}$ for any $\lambda > 0$. The parameter λ is chosen to balance the smoothing strength with the error; in our experiments, we obtained good performance with $1 \leq \lambda \leq 5$. We use sparse arrays for the large matrices to improve computational efficiency.

Piecewise Linear Off-Resonance Correction

Once the field map coefficients are known, Eq. 5 suggests the following piecewise correction strategy for each padded block (Fig. 2): warp the corrupted data to correct the trajectory shift and then remove the undesired phase modulation with a conjugate phase multiplication (5). We perform these operations on $s_{\mathrm{o}}(k'_x, k'_y)$, the k-space data from the padded block, using the smoothed coefficients for the block from $\boldsymbol{c}_{\boldsymbol{s}}$. After correction and inverse Fourier transformation, the padded regions are discarded and the blocks are recombined to form the final deblurred image. This locally first-order strategy can provide better image quality than locally zeroth-order methods in regions containing fine anatomical details and rapidly varying off-resonance (15).

In our experiments, the trajectory shift was not significant enough to necessitate correction of the density compensation function. For larger shifts, postgridding compensation as described by Irarrazaval et al. (5) could be applied to the block although Chen and Meyer (8) noted limitations with deapodization in this approach. A more accurate but computationally expensive alternative for correcting a block is to reconstruct an entire image by regridding the raw spiral data with the shifted trajectory and commensurately adjusted density weighting, and then retaining only the pixels belonging to the block.

METHODS

We performed fine-resolution spiral imaging of a phantom and cardiovascular scans of healthy volunteers. All volunteers were screened for contraindications and provided informed consent in accordance with institutional policy. Experiments were performed on a Signa Excite HD 3T system (GE Healthcare, Waukesha, WI) with 40 mT/m maximum gradient amplitude, 150 T/m/s maximum slew rate, and 4 μs receiver sampling interval. We acquired 2D multislice spoiled gradient echo scans with uniform-density spiral trajectories and 55° spectral spatial RF excitation (16) to attenuate signal from fat. The slice thickness was 5.0 mm and three to five slices were acquired per scan. All acquisitions used body coil transmission and an eight-channel phased array cardiac coil for reception, and were preceded by automatic prescan calibration and gradient shimming. Motion artifacts were controlled with breath holding and ECG gating. Spiral images were initially reconstructed using gridding with Jacobian density compensation (17) and inverse Fourier transformation. Multicoil data were combined with phase-sensitive reconstruction (18); parallel imaging was not used. Data processing was performed with Matlab (Mathworks, Natick, MA).

One spiral shot was acquired for each echo per slice per heartbeat. The TR varied between 700 and 1100 ms depending on the volunteer's heart rate. Two echoes were acquired to create field maps to compare our method with field map-based correction. The second echo was acquired immediately after the first to minimize registration errors from motion. An echo spacing of 1.6 ms was used to produce field maps with 625 Hz of off-resonance bandwidth, which was chosen to avoid frequency aliasing due to phase wrapping. Trajectory parameters for the first echo were 16 shots, TE = 2.0 ms, and δ = 0.7–1.0 mm. Note that δ is the error-free resolution, or the point spread function mainlobe width in the absence of off-resonance. Parameters for the second echo were 16 shots, TE = 3.6 ms, and δ = 2.0 mm. The FOV was 22.0–28.0 cm depending on size of the volunteer, resulting in T_{read} durations of 15.9–25.6 ms for the first echo and 3.6–4.3 ms for the second. For the phantom scan, FOV = 16 cm, δ = 0.5 mm for the image, and δ = 2.0 mm for the field map.

We compared piecewise linear autofocus with conventional autofocus and field map-based off-resonance correction in 15 data sets from eight volunteers. Piecewise linear autofocus was run with a 5×5 block padded to 40×40 ($\mathrm{FOV_b}$ = 3.5–5.0 mm and $\mathrm{FOV_p}$ = 28–40 mm), Gaussian window with standard deviation $\mathrm{FOV_p}/2$, and smoothing parameter $\lambda = 2$. These values were experimentally determined based on data from two volunteers and subsequently used for all data sets. With multicoil data, we independently estimated the local field map coefficients for each channel and then averaged the coefficients with weights derived from the total channel energy in the block. For field-map based deblurring, we used frequency-segmented conjugate phase reconstruction (1) with $4(f_{\max} - f_{\min})T_{\mathrm{read}}$ demodulation frequencies (4). Chen and Meyer (11) observed no visible differences between this and other methods of conjugate phase reconstruction. Field maps were generated from the second echo and the central k-space region of the first echo. For conventional autofocus, we used the method by Noll et al. (6) with the improved objective function proposed by Lee et al. (10). The data were demodulated with the same set of demodulation frequencies used by field map-based deblurring; normally the minimum and maximum frequencies would be guessed, but without this knowledge a priori the spurious minima often confused the optimization and exacerbated the off-resonance artifacts. Before evaluating the focus metric, the low pass image phase was removed from each demodulated image. The low pass cutoff frequency k_{lo} was manually adjusted for each data set to give the best performance. The integration window was similarly tailored to each data set. As with the proposed autofocus method, the frequency estimates from multiple coils were combined with weighted averaging.

RESULTS

Conventional autofocus yielded a variable improvement in image quality. Every image contained obvious residual blurring artifacts, and several images showed exacerbated artifacts despite the efforts to boost the algorithm's performance. Furthermore, deblurring performance was

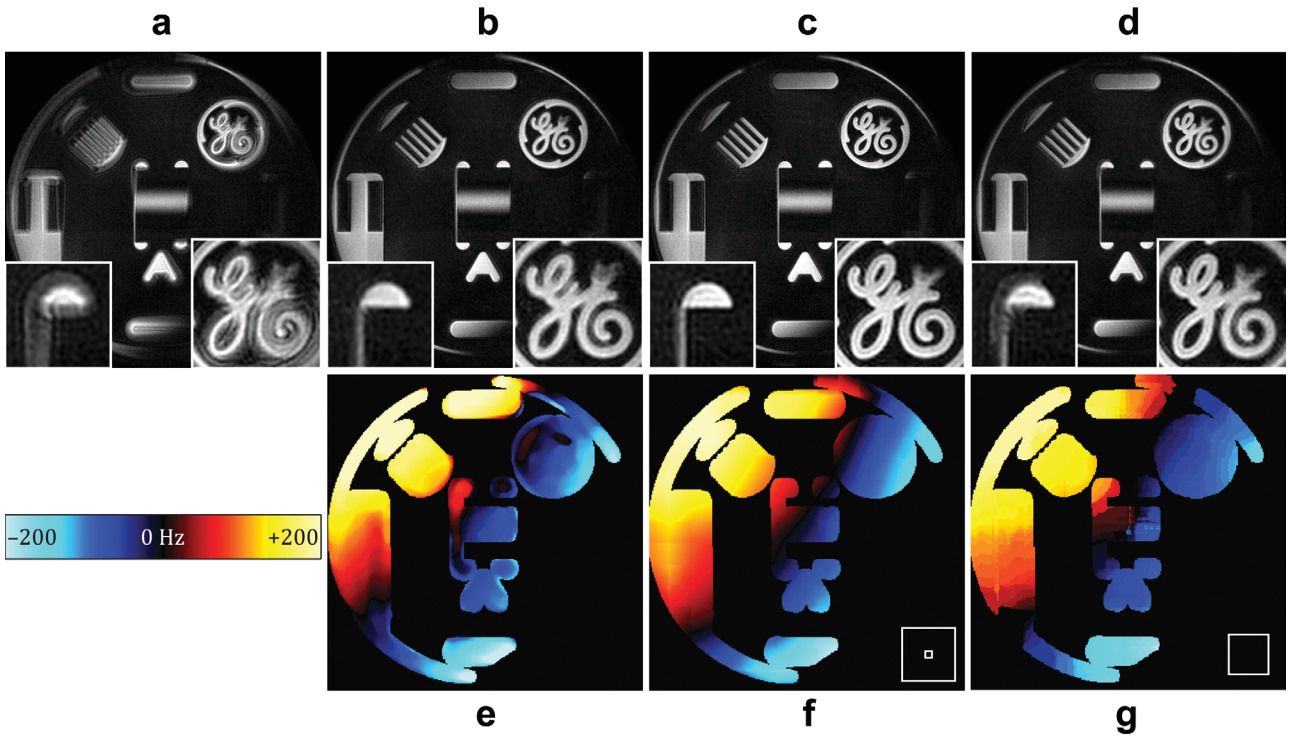

FIG. 4. Comparison of different off-resonance correction methods in a spiral scan of a phantom. The bottom corners in (a–d) show zoomed-in results. **a**: Original image without off-resonance correction. This is the input to the proposed autofocus algorithm. **b**: Image after correction with the measured field map (e) using frequency-segmented conjugate phase reconstruction. Minor residual blurring due to uncorrected off-resonance is visible. **c**: Image after piecewise linear autofocus. Off-resonance artifacts are not apparent. **d**: Image after conventional optimization-based autofocus. Some residual off-resonance artifacts remain. **e**: The measured field map. **f**: The estimated piecewise linear field map. The block sizes (with and without padding) are shown in the lower right. **g**: The estimated field map from conventional autofocus. The integration window size is shown in the lower right. [Color figure can be viewed in the online issue, which is available at wileyonlinelibrary.com.]

inconsistent in anatomically similar regions from different volunteers.

In comparison, field map-based conjugate phase reconstruction provided consistently good deblurring performance in every data set, as expected. In several images, minor residual blurring was still apparent.

Piecewise linear autofocus provided better off-resonance correction than conventional autofocus for every data set, and in most cases its images were comparable to field map-based deblurring. Of the images deblurred by the proposed method, most contained at least one region that was obviously sharper than the corresponding region in the conjugate phase reconstructed image, and about half contained some slight residual blurring. We observed no instances of exacerbated off-resonance artifacts, however.

Phantom results are shown in Fig. 4. Figure 4a is the original blurry image. Figure 4b is the result of conjugate phase reconstruction and shows effective off-resonance correction although some residual blurring is visible. Figure 4c is the image after piecewise linear autofocus and shows no residual blurring artifacts, most likely because of the strong image contrast. Figure 4d is the image after conventional autofocus with $k_{lo} = 0.01/\delta$ and a 30×30 integration window and shows minor residual artifacts. Figure 4e–g shows the field maps from measurement, estimation by the proposed method, and estimation by conventional autofocus, respectively. When the estimated piecewise linear field map is used with conjugate phase reconstruction instead of piecewise linear correction, the resulting image is almost identical to that in Fig. 4c. This suggests the field map estimated by the proposed algorithm is more accurate than the measured one.

Figure 5 shows representative deblurring results with $\delta = 0.7$ mm spiral imaging. For this scan, FOV = 22 cm and $T_{read} = 20.1$ ms. Figure 5a is the original image without off-resonance correction. Figure 5b is the image after conjugate phase reconstruction and shows minor residual blurring around the spine and aorta. Figure 5c is the image after piecewise linear autofocus. The image is visually comparable to the result from field map-based correction. Minor residual blurring is apparent in the chest wall, but regions near the aorta and spine appear sharper in the autofocused image. Figure 5d is the image after conventional autofocus with $k_{lo} = 0.05/\delta$ and a 50×50 integration window. The chest wall appears slightly sharper than with the proposed algorithm, but moderate residual blurring is apparent near the spine and coronary artery. We applied the two-stage approach by Man et al. (7) to correct these residual artifacts, but found no improvement in image quality. Figure 5e–g shows the field maps from measurement, estimation by the proposed method, and estimation by conventional autofocus, respectively. The agreement between the field map estimated by the proposed method and the

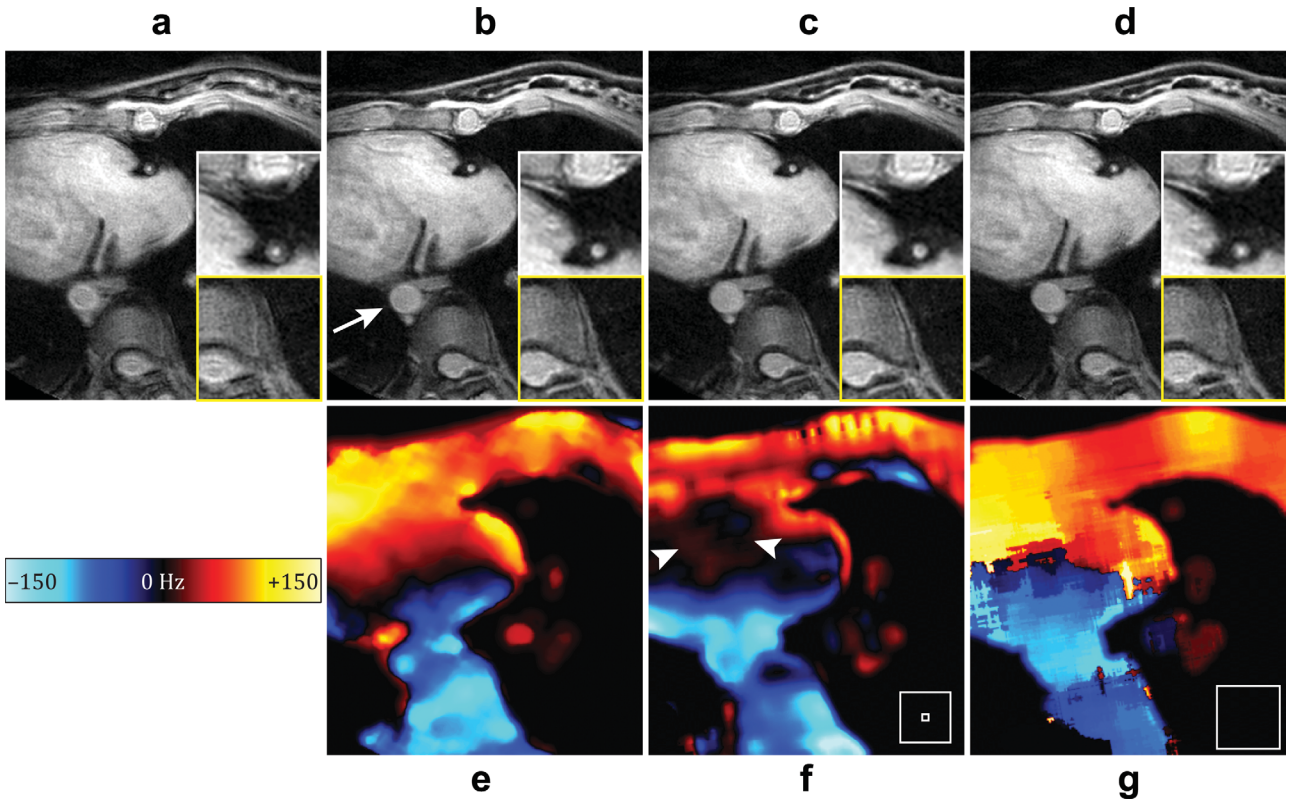

FIG. 5. Comparison of different off-resonance correction methods in a spiral cardiac scan of a healthy volunteer. Zoomed-in areas near the coronary artery (white box) and spine (yellow box) are shown along the right edge in (a–d). **a**: Original image without off-resonance correction. **b**: Image after correction with the measured field map (e) using frequency-segmented conjugate phase reconstruction. Some slight blurring is still apparent around the aorta (arrow). **c**: Image after piecewise linear autofocus. The result is comparable to the field map-based deblurring. **d**: Image after conventional optimization-based autofocus. Residual off-resonance artifacts are obvious. **e**: The measured field map. **f**: The estimated piecewise linear field map. In featureless regions (arrowheads), the field map is underestimated although this is not problematic. The block sizes (with and without padding) are shown in the lower right. **g**: The estimated field map from conventional autofocus. The integration window size is shown in the lower right. [Color figure can be viewed in the online issue, which is available at wileyonlinelibrary.com.]

measured field map is poor in featureless regions regions due to underestimation of the local constant coefficients. However, the residual blurring from uncorrected off-resonance in these areas is not apparent.

Deblurring results using data from only one coil are shown in Fig. 6. The signal from the right coronary artery has low SNR because of the reduced sensitivity in the posterior receiver coil. Figure 6b shows the original, uncorrected single-coil image. Figure 6c is the image after conjugate phase reconstruction using the field map derived from the full multi-coil data (Fig. 5e). Figure 6d is the image after piecewise linear autofocus and is similar to the result from field map-based correction. Figure 6e is the image after conventional autofocus and shows no improvement over the original image. The SNR in the coronary cross-section is approximately 3.5 in the original image, 5.0 after conjugate phase reconstruction, 4.7 after piecewise linear autofocus, and 3.4 after conventional autofocus.

As shown in Figs. 4 and 5, the proposed autofocus algorithm can produce better image quality than field map-based conjugate phase reconstruction. We explored two possible reasons for this: the field map estimate may

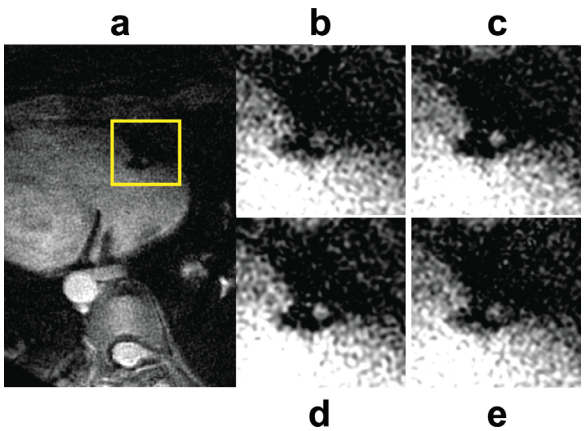

FIG. 6. Off-resonance correction of low-SNR data. **a**: Full image from one coil showing a low SNR region around the right coronary artery (yellow box). **b**: No off-resonance correction (coronary SNR = 3.5). **c**: Correction with frequency-segmented conjugate phase reconstruction using the measured field map (SNR = 5.0). **d**: Correction with piecewise linear autofocus (SNR = 4.7). The result is similar to field map-based correction. **e**: Correction with conventional autofocus (SNR = 3.4). The images in (b–d) have been clipped to show more detail. [Color figure can be viewed in the online issue, which is available at wileyonlinelibrary.com.]

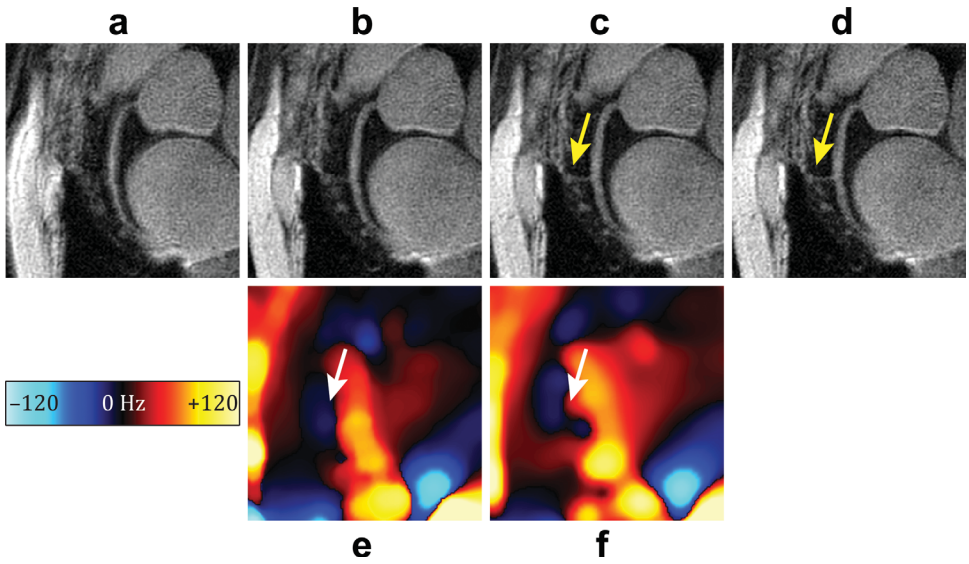

FIG. 7. Field map measurement inaccuracy and higher-order correction. **a**: No off-resonance correction. **b**: Image after correction with frequency-segmented conjugate phase reconstruction using the measured field map (e). **c**: Image after correction with frequency-segmented conjugate phase reconstruction using the estimated piecewise linear field map (f). Deblurring with the estimated field map reveals more details (arrow). **d**: Image after correction with the proposed autofocus algorithm (piecewise linear correction using the estimated piecewise linear field map, f). The higher-order off-resonance correction recovers finer-scale details. **e**: The measured field map. **f**: The estimated piecewise linear field map. [Color figure can be viewed in the online issue, which is available at wileyonlinelibrary.com.]

be more accurate than measurement (Fig. 7b,c), and piecewise linear correction may provide more accurate correction than locally zeroth-order methods (Fig. 7c,d). In our experiments, we found more evidence supporting the former reason and only a few examples of the latter. In most cases when our autofocus algorithm provided superior sharpness, we could greatly close the gap in image quality by rerunning conjugate phase reconstruction with the estimated piecewise linear field map. Only in rare cases were the anatomical features fine enough and the off-resonance variations large enough that we could attribute the sharpness enhancement solely to the higher-order correction (Fig. 7d). Although the piecewise linear framework imparts robustness to the field map estimation stage, its necessity in the correction stage requires further investigation. Nonetheless, we did not find evidence that piecewise linear correction produced results worse than conjugate phase reconstruction when both methods were run with the same field map.

DISCUSSION

Piecewise linear autofocus is noise robust because of its two estimation strategies. The local linear coefficients are estimated from the spectral peak, which has the highest SNR of all acquired *k*-space data. During the estimation of local constant coefficients, errors are reduced by the inherent averaging within the correlation operation and by averaging the results from the two strips.

The proposed algorithm requires only the blurry complex image and the trajectory time map as inputs. In our experiments, we supplied the coil-separated images, but the algorithm also accepts coil-combined images. As it does not require access the raw *k*-space data, it can be easily incorporated into existing image reconstruction pipelines. The final deblurred complex images are compatible with other artifact correction methods and postprocessing techniques.

The proposed autofocus algorithm is easier to use than conventional autofocus, which has many tuning parameters—including the integration window size, choice of demodulation frequencies, low-pass cutoff frequency for phase removal, and possibly multi-scale block sizes (7)—which preclude truly automatic use. In comparison, the primary tuning parameter for piecewise linear autofocus is the block size. We obtained good results without having to manually adjust parameters for every data set.

There are several considerations when choosing the block size. Smaller blocks yield better spatial resolution in the estimated field map and reduce intrablock averaging of rapidly varying off-resonance. Larger blocks provide better frequency resolution for locating the spectral peak, and usually contain more image features to correlate. We generally suggest block sizes where $\mathrm{FOV_b}$ is two tot three times larger than the smallest resolvable structures, and $\mathrm{FOV_p}$ is at least $5 \times \mathrm{FOV_b}$. The block size also bounds the frequency estimates. With mapdrift, the maximum measurable constant coefficient is $\pm \mathrm{FOV_p}/4\delta T_{\mathrm{read}}$, which corresponded to around ± 400 Hz in our experiments and was large enough to accommodate the off-resonance typically observed in the heart (19). To correct greater off-resonance, we suggest a multistage approach in which larger blocks are used first followed by smaller blocks to correct the residual off-resonance.

As shown in Eq. 7, the linear coefficient estimation requires a nonzero echo time. The estimation accuracy will improve as TE increases and the spectral peak location becomes more dominated by TE. The TE bounds the maximum measurable linear coefficient at $\pm 1/2\delta \mathrm{TE}$,

which corresponds to a shift of the spectral peak to the edge of the acquired *k*-space support. In our experiments, this bound was around 350 Hz/mm, which is large enough to accommodate any realistic imaging scenario. Usually, the trajectory will overlap itself before the peak is shifted to the edge. Overlaps cannot be compensated by any off-resonance correction method because colocated *k*-space data cannot be separated. Nonetheless, the spectral peak should still be detectable and the trajectory shift can be at least partially corrected.

Auxiliary sources of linear image-domain phase—such as the receiver coil—will shift the location of the spectral peak and bias the linear coefficient estimation. We did not observe bias problems in our experiments with the block sizes we used. In general, small blocks could worsen the bias because over a smaller region any spatially smooth auxiliary phase will more likely have a significant linear component. However, with sufficiently smooth phase or small enough blocks, the phase within a block will become an inconsequential constant offset. Furthermore, in our two-step estimation strategy, errors in the estimated linear coefficients can be offset by the constant coefficient.

In image regions with few features or low contrast, there will be little information to correlate and the mapdrift approach will underestimate f_c. Similar limitations have been observed in other off-resonance correction algorithms (6,11). In magnitude images, this is not problematic because the uncorrected blurring artifacts will not be obvious. If residual off-resonance in these regions is an issue for phase images, then the block size can be increased to include nearby anatomical structure at the expense of field map resolution.

The proposed autofocus algorithm is more computationally demanding than conventional autofocus methods. With our unoptimized Matlab implementation, the average processing time for a 360×360 pixel image was 56 s on a single-core 2.9 GHz CPU. In contrast, the average times for conjugate phase reconstruction and conventional autofocus were 0.8 and 10 s, respectively. The estimation stage accounted for approximately 90% of the run time of our algorithm, with the dominant operation being the Fourier transform. Faster times are possible by porting to a compiled language. The algorithm is naturally parallelizable because each block and coil is processed independently, making further speed improvements obtainable on multiprocessor systems.

The proposed algorithm could be extended in several ways. Mapdrift accuracy can be improved by averaging results from more than two directions. A higher-order field map model may also be possible. The approach suggested by Parot et al. (20) may be useful in performing piecewise quadratic deblurring. By processing the entire image as one block, the proposed method becomes a robust alternative to optimization-based automatic global linear correction (8). Finally, although we have discussed its use with 2D spiral trajectories, it extends straightforwardly to radial and 3D trajectories so long as the time map varies monotonically with *k*-space radius.

CONCLUSION

Piecewise linear autofocus, a physics-based automatic off-resonance correction method, has been developed to overcome limitations related to conventional approaches that require optimization of a heuristic objective function. Local linear field map estimation and off-resonance correction are performed on the blurry image. The piecewise linear framework provides robust field map estimation and noise tolerance. Off-resonance correction of fine-resolution spiral data indicates that the proposed method can be more accurate than conventional autofocus and comparable to field map-based methods.

ACKNOWLEDGMENTS

The authors thank the reviewers for their comments and suggestions. This work was supported by an award from the American Heart Association.

REFERENCES

1. Noll DC, Meyer CH, Pauly JM, Nishimura DG, Macovski A. A homogeneity correction method for magnetic resonance imaging with time-varying gradients. IEEE Trans Med Imaging 1991;10:629–637.
2. Man LC, Pauly JM, Macovski A. Multifrequency interpolation for fast off-resonance correction. Magn Reson Med 1997;37:785–792.
3. Kadah YM, Hu X. Simulated phase evolution rewinding (SPHERE): a technique for reducing B0 inhomogeneity effects in MR images. Magn Reson Med 1997;38:615–627.
4. Moriguchi H, Dale BM, Lewin JS, Duerk JL. Block regional off-resonance correction (BRORC): a fast and effective deblurring method for spiral imaging. Magn Reson Med 2003;50:643–648.
5. Irarrazaval P, Meyer CH, Nishimura DG, Macovski A. Inhomogeneity correction using an estimated linear field map. Magn Reson Med 1996;35:278–282.
6. Noll DC, Pauly JM, Meyer CH, Nishimura DG. Deblurring for non-2D Fourier transform MRI. Magn Reson Med 1992;25:319–333.
7. Man LC, Pauly JM, Macovski A. Improved automatic off-resonance correction without a field map in spiral imaging. Magn Res Med 1997;37:906–913.
8. Chen W, Meyer CH. Fast automatic linear off-resonance correction method for spiral imaging. Magn Reson Med 2006;56:457–462.
9. Truong TK, Chen NK, Song AW. Application of k-space energy spectrum analysis for inherent and dynamic B0 mapping and deblurring in spiral imaging. Magn Reson Med 2010;64:1121–1127.
10. Lee D, Nayak KS, Pauly JM. Reducing spurious minima in automatic off-resonance correction for spiral imaging. In: Proceedings of the International Society of Magnetic Resonance in Medicine, Kyoto, Japan, 2004. p.2678.
11. Chen W, Meyer CH. Semiautomatic off-resonance correction in spiral imaging. Magn Reson Med 2008;59:1212–1219.
12. Dahnke H, Liu W, Herzka D, Frank JA, Schaeffter T. Susceptibility gradient mapping (SGM): a new postprocessing method for positive contrast generation applied to superparamagnetic iron oxide particle (SPIO)-labeled cells. Magn Reson Med 2008;60:595–603.
13. Mancill CE, Swiger JM. A map drift autofocus technique for correcting higher order SAR phase errors. Annual Tri-Service Radar Symposium Record, Monterey, CA, 1981. pp.391–400.
14. Boyd S, Vandenberghe L. Convex optimization. New York: Cambridge University Press;2004.
15. Smith TB, Nayak KS. Recovering fine-scale features in spiral imaging with piecewise linear off-resonance correction. In: Proceedings of the International Society of Magnetic Resonance in Medicine, Montreal, Canada, 2011. p.4579.
16. Meyer CH, Pauly JM, Macovski A, Nishimura DG. Simultaneous spatial and spectral selective excitation. Magn Reson Med 1990;15:287–304.
17. Hoge RD, Kwan RK, Pike GB. Density compensation functions for spiral MRI. Magn Reson Med 1997;38:117–128.
18. Bernstein MA, Grgic M, Brosnan TJ, Pelc NJ. Reconstructions of phase contrast, phased array multicoil data. Magn Reson Med 1994;32:330–334.
19. Sung K, Nayak KS. Design and use of tailored hard pulse trains for uniformed saturation of myocardium at 3 Tesla. Magn Reson Med 2008;60:997–1002.
20. Parot V, Sing-Long C, Lizama C, Tejos C, Uribe S, Irarrazaval P. Application of the fractional Fourier transform to image reconstruction in MRI. Magn Reson Med. 2011. doi: 10.1002/mrm.23190.